

# Terahertz single pixel imaging with an optically controlled dynamic spatial light modulator

David Shrekenhamer, Claire M. Watts, and Willie J. Padilla\*

Department of Physics, Boston College, 140 Commonwealth Ave., Chestnut Hill, MA 02467, USA

\*[willie.padilla@bc.edu](mailto:willie.padilla@bc.edu)

**Abstract:** We present a single pixel terahertz (THz) imaging technique using optical photoexcitation of semiconductors to dynamically and spatially control the electromagnetic properties of a semiconductor mask to collectively form a THz spatial light modulator (SLM). By co-propagating a THz and collimated optical laser beam through a high-resistivity silicon wafer, we are able to modify the THz transmission in real-time. By further encoding a spatial pattern on the optical beam with a digital micro-mirror device (DMD), we may write masks for THz radiation. We use masks of varying complexities ranging from 63 to 1023 pixels and are able to acquire images at speeds up to 1/2 Hz. Our results demonstrate the viability of obtaining real-time and high-fidelity THz images using an optically controlled SLM with a single pixel detector.

© 2013 Optical Society of America

**OCIS codes:** (110.6795) Terahertz imaging; (160.3918) Metamaterials; (070.6120) Spatial light modulators; (110.1085) Adaptive imaging.

---

## References and links

1. D. M. Mittleman, M. Gupta, R. Neelamani, R. G. Baraniuk, J. V. Rudd, and M. Koch, "Recent advances in terahertz imaging," *Appl. Phys. B* **68**, 1085–1094 (1999).
2. W. L. Chan, J. Deibel, and D. M. Mittleman, "Imaging with terahertz radiation," *Rep. on Prog. in Phys.* **70**, 1325–1379 (2007).
3. T. M. Korter and D. F. Plusquellic, "Continuous-wave terahertz spectroscopy of biotin: vibrational anharmonicity in the far-infrared," *Chem. Phys. Lett.* **385**, 45–51 (2004).
4. N. Karpowicz, H. Zhong, C. Zhang, K. -I. Lin, J. -S. Hwang, J. Xu, and X. -C. Zhang, "Compact continuous-wave subterahertz system for inspection applications," *Appl. Phys. Lett.* **86**, 054105 (2005).
5. K. Kawase, Y. Ogawa, Y. Watanabe, and H. Inoue, "Non-destructive terahertz imaging of illicit drugs using spectral fingerprints," *Opt. Express* **11**, 2549 (2003).
6. G. P. Williams, "Filling the THz gap – high power sources and applications," *Rep. Prog. Phys.* **69**, 301–326 (2005).
7. A. W. Lee, and Q. Hu, "Real-time, continuous-wave terahertz imaging by use of a microbolometer focal-plane array," *Opt. Lett.* **30**, 2563–2565 (2005).
8. N. R. Butler, R. J. Blackwell, R. Murphy, R. J. Silva, and C. A. Marshall, "Low-cost uncooled microbolometer imaging system for dual use," *Proc. SPIE* **2552** 583–591 (1995).
9. Q. Wu, T. D. Hewitt, and X. -C. Zhang, "Two-dimensional electro-optic imaging of THz beams," *Appl. Phys. Lett.* **69**, 1026–1028 (1996).
10. B. B. Hu and M. C. Nuss, "Imaging with terahertz waves," *Opt. Lett.* **20**, 1716–1718 (1995).
11. M. C. Nuss, "Chemistry is right for T-ray imaging," *IEEE Circ. Dev. Mag.*, **12**, 25–30 (1996).
12. W. L. Chan, K. Charan, D. Takhar, K. F. Kelly, R. G. Baraniuk, and D. M. Mittleman, "A single-pixel terahertz imaging system based on compressed sensing," *Appl. Phys. Lett.* **93**, 121105 (2008).
13. O. Furchi, E. L. Jacobs, and C. Preza, "Image plane coded aperture for terahertz imaging," *Opt. Eng.* **51**, 091612 (2012).

14. H. Shen, L. Gan, N. Newman, Y. Dong, C. Li, Y. Huang, and Y. Shen, "Spinning disk for compressive imaging," *Opt. Lett.* **37**, 46–48 (2012).
15. D. Dudley, W. Duncan, and J. Slaughter, "Emerging digital micromirror device (DMD) applications," *Proc. SPIE* **4985**, 14–25 (2003).
16. K. M. Johnson, D. J. McKnight, and I. Underwood, "Smart spatial light modulators using liquid crystals on silicon," *IEEE J. Quantum Electron.* **29**, 699–714 (1993).
17. M. Rahm, J. Li, and W. J. Padilla, "THz wave modulators: a brief review on different modulation techniques," *J. Infrared Millim. Terahz. Waves* **34**, 1–27 (2012).
18. W. L. Chan, H. -T. Chen, A. J. Taylor, I. Brener, M. J. Cich, and D. M. Mittleman, "A spatial light modulator for terahertz beams," *Appl. Phys. Lett.* **94**, 213511 (2009).
19. D. Shrekenhamer, S. Rout, A. C. Strikwerda, C. Bingham, R. D. Averitt, S. Sonkusale, and W. J. Padilla, "High speed terahertz modulation from metamaterials with embedded high electron mobility transistors," *Opt. Express* **19**, 9968–9975 (2011).
20. G. W. Webb, W. Vernon, M. Sanchez, S. Rose, and S. Angello, "Optically controlled millimeter wave antenna," *Microw. Photon.* 275–278 (1999).
21. M. R. Chaharmir, J. Shaker, M. Cuhaci, and A. Sebak, "Novel photonic-controlled reflectarray antenna," *IEEE Trans. Antennas Propag.* **54**, 1134–1141 (2006).
22. X. C. Zhang and D. Auston, "Generation of steerable submillimeter waves from semiconductor surfaces by spatial light modulators," *Appl. Phys. Lett.* **59**, 768–770 (1991).
23. T. Okada and K. Tanaka, "Photo-designed terahertz devices," *Sci. Rep.* **1**, 121 (2011).
24. S. Busch, B. Scherger, M. Scheller, and M. Koch, "Optically controlled terahertz beam steering and imaging," *Opt. Lett.* **37**, 1391–1393 (2012).
25. M. Harwit and N. J. Sloane, *Hadamard Transform Optics* (Academic, 1979).
26. W. Cheney and D. Kincaid, *Numerical Mathematics and Computing*, 6<sup>th</sup> ed. (Thompson Brooks/Cole, 2008).
27. R. H. Bube, *Photoelectronic Properties of Semiconductors*, (Cambridge University, 1992).
28. D. Cooke and P. U. Jepsen, "Optical modulation of terahertz pulses in a parallel plate waveguide," *Opt. Express* **16**, 15123–15129 (2008).
29. M. Van Exter and D. Grischkowsky, "Optical and electronic properties of doped silicon from 0.1 to 2 THz," *Appl. Phys. Lett.* **56**, 1694–1696 (1990).
30. H. Alius and G. Dodel, "Amplitude-, phase-, and frequency modulation of far-infrared radiation by optical excitation of silicon," *Infrared Phys.* **32**, 1–11 (1991).
31. T. Jeon and D. Grischkowsky, "Nature of conduction in doped silicon," *Phys. Rev. Lett.* **78**, 1106–1109 (1997).
32. H. Schulenburg and H. Tributsch, "Electropassivation of silicon and bulk lifetime determination with dry polymer contact," *J. Phys. D* **33**, 851 (2000).
33. C. Hutley, *Diffraction Gratings*, (Academic, 1982).
34. J. P. Rice, J. E. Neira, M. Kehoe, and R. Swanson, "DMD diffraction measurements to support design of projectors for test and evaluation of multispectral and hyperspectral imaging sensors," *Proc. SPIE* **7210**, 72100D (2009).
35. E. L. Shirley, "Diffraction effects on broadband radiation: formulation for computing total irradiance," *Appl. Opt.* **43**, 2609–2620 (2004).
36. C. A. Bennet, *Principles of Physical Optics* (John Wiley & Sons, 2008).
37. W. J. Padilla, A. J. Taylor, C. Highstrete, M. Lee, and R. D. Averitt, "Dynamical electric and magnetic metamaterial response at terahertz frequencies," *Phys. Rev. Lett.* **96**, 107401 (2006).
38. H. -T. Chen, W. J. Padilla, M. J. Cich, A. K. Azad, R. D. Averitt, and A. J. Taylor, "A metamaterial solid-state terahertz phase modulator," *Nat. Photonics* **3**, 148–151 (2009).
39. H. Chen, J. F. O'Hara, A. J. Taylor, R. D. Averitt, C. Highstrete, M. Lee, and W. J. Padilla, "Complementary planar terahertz metamaterials," *Opt. Express* **15**, 1084–1095 (2007).
40. R. A. DeVerse, R. R. Coifman, A. C. Coppi, W. G. Fateley, F. Geshwind, R. M. Hammaker, S. Valenti, F. J. Warner, and G. L. Davis, "Application of spatial light modulators for new modalities in spectrometry and imaging," *Proc. SPIE* **4959**, 12–22 (2003).

---

## 1. Introduction

Terahertz (THz) radiation has great potential for imaging applications [1, 2] due to its ability to penetrate most dielectric materials and non-polar liquids. Its harmless interaction with human tissue suggests imaging in this regime has immediate applicability in the fields of biodetection [3], system inspection [4], and detection of illegal drugs [5]. However, a significant limitation currently preventing wide-spread THz imaging is the absence of efficient sources and detectors operating between 0.1 and 10 THz - a band of the electromagnetic spectrum often referred to as the "THz gap" [6]. Although there exists great technical difficulty in feasibly

performing THz imaging, there has been moderate progress over the past 25 years. Multi-element detector schemes, both microbolometer arrays [7, 8] and electro-optic sampling with high-performance CCD cameras [9], provide accurate and real-time THz images. However, these imaging systems often require high powered sources and/or expensive complex detectors that lack the sensitivity of single element detectors. The use of a single detector has been employed to obtain THz images by mechanically raster scanning the object plane to acquire spatial information [10]. While the latter technique has the benefit of high spatial resolution and accurate imaging, major shortcomings are the long acquisition time [11] and the mechanical nature of the scanning system.

An alternative single pixel solution - relying on spatial multiplexing - could help overcome many of the disadvantages involved with more conventional imaging techniques. The imaging of complex scenes is enabled with sparse detector arrays or even single pixels using spatial light modulators (SLMs) to multiplex the image. Mechanical masks that are either manually exchanged or placed onto spinning discs have demonstrated proof of principle THz imaging using, for example, compressive sensing and adaptive coded aperture imaging [12–14]. Although SLMs, such as digital micro-mirror (DMD) [15] and liquid crystal (LC) [16] systems are commercially available, they do not operate at THz frequencies. Attempts to develop THz SLMs have thus far been ineffective in producing efficient and high speed devices, though there are several attractive alternatives to using mechanical masks.

Semiconductor and metamaterial / semiconductor hybrid devices can be controlled by a variety of different methods to achieve THz amplitude and frequency modulation [17]. An initial study demonstrated performance of a room-temperature electronic controlled metamaterial for a  $4 \times 4$  pixel array used to form a diffractive grating [18]. Additionally, all-electronic dynamic metamaterials have demonstrated switching speeds up to 10 MHz [19]. Another avenue to achieving a THz SLM has been inspired by the work initially developed at millimeter wavelengths where optically excited electron plasmas in photo-active semiconductors serve as a spatial mask in creating Fresnel lenses and reflect-arrays for beam-steering and communication based applications [20, 21]. Early studies indicate that THz spatial modulation is also possible with sufficient optical power [22–24]. Both electronic and optically controlled SLMs pose as a fast and efficient means to dynamically control electromagnetic radiation thus allowing for realistic methods to perform THz imaging.

In this work we demonstrate single pixel multiplex THz imaging based on an optically controlled reconfigurable THz mask in high-resistivity Silicon ( $\rho$ -Si). By utilizing a DMD to optically encode spatial patterns we are able to achieve up to 1023-pixel, high fidelity THz images with frame rates as fast as one image per two seconds - only limited by available software. The achieved signal-to-noise ratio (SNR) suggests the possibility that our technology may provide quasi real-time THz imaging with frame rates as fast as 3 frames per second (fps).

## 2. Theory

### 2.1. Imaging theory

Typical single pixel camera architectures involve four key components: a light source, imaging optics, a single element detector, and a SLM. Light from an illuminated object is focused using imaging optics onto a SLM which, for binary encoding, selectively passes portions of the image to the detector and blocks others. A sequence of known patterns is displayed on the SLM and a single value is acquired for each mask frame. Prior knowledge of these masks allows for the reconstruction of the image as schematically illustrated in Fig. 1. For example, mechanical raster scanning can be emulated by displaying a single pixel at a time on the SLM.

For imaging systems using intensity based detectors that are not sensitive to the phase of electromagnetic radiation, binary masks that modulate the intensity are well suited. There are sev-

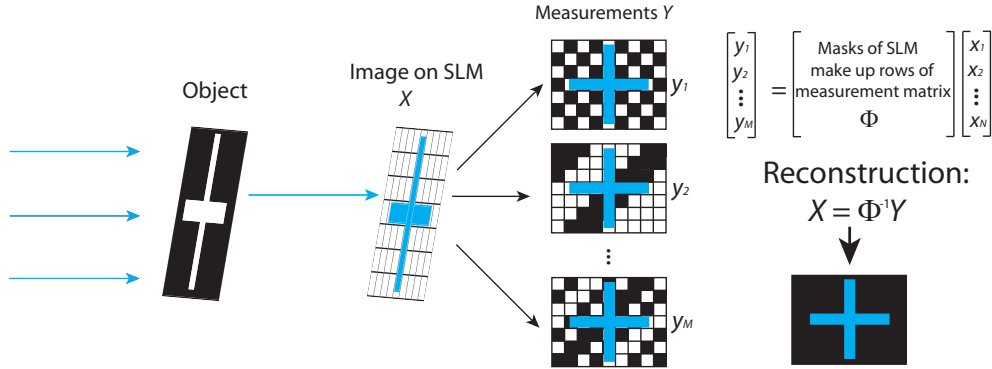


Fig. 1. Schematic depicting multiplex imaging process where the spatial modulation of a formed image allows for the reconstruction using a single pixel detector. Example  $7 \times 9$  binary masks taken from rows of the  $63 \times 63$   $S$ -matrix are shown.

eral different types of binary coded apertures that can be used to multiplex an image - though the field is dominated by random and Hadamard based masks. Random binary masks are comprised of 1's and 0's determined by standard probability distributions such as Gaussian or Bernoulli, among others. Hadamard matrices are square matrices composed of +1's and -1's in which each row is orthogonal to all other rows [25]. To create binary masks we can use an  $S$ -matrix, created by omitting the first row and column of the corresponding normalized Hadamard matrix, substituting all 1's with 0's, and all -1's with 1's. Each row of this matrix can then be used as a 1, 0 mask for successive measurements in a single pixel imaging system.

We define a one- or two- dimensional image by a vector  $X$  with  $N$ -elements (this can be done by concatenating the rows into a single column). We represent a single measurement  $y_j$  in a multiplexing scheme by the following expression:

$$y_j = \sum_{i=1}^N \phi_{ji} x_i \quad (1)$$

or the matrix equation  $Y = \Phi \times X$ . In this equation,  $Y$  is a column vector with  $M$ -elements representing the  $M$  measurements taken and  $\Phi$  is the  $M \times N$  measurement matrix, in which each row represents a mask displayed on the SLM. For example,  $\Phi$  that corresponds to a raster scan imaging technique is the  $N \times N$  identity matrix. For a well-conditioned measurement matrix [26] and the fully determined case, i.e.  $M = N$ , the reconstruction becomes linear and can be solved by a simple matrix equation:  $X = \Phi^{-1} \times Y$  [25]. One advantage of using  $S$ -matrices as the measurement matrix such that  $\Phi = S_N$  is the particularly simple decoding process given by:  $S_N^{-1} = \frac{2}{N+1}(2S_N^T - J_N)$  where  $S_N$  is the  $S$ -matrix of order  $N$ ,  $S_N^T$  is its transpose, and  $J_N$  is an  $N \times N$  matrix of all 1's [25].

## 2.2. Dynamic THz spatial light modulators

The photoexcitation of free carriers in semiconductors is a well understood process for both CW and ultrafast optical beams [27]. For  $p$ -Si substrates a higher carrier density can be generated by CW pump beams, compared to pulsed sources of identical average power, due to the relatively long carrier lifetimes in Si [28]. The change in the complex dielectric constant can be described by the Drude model [28–31].

$$\varepsilon(\omega) = \varepsilon_\infty - \frac{\omega_p^2}{\omega(\omega + i\Gamma)}, \quad (2)$$

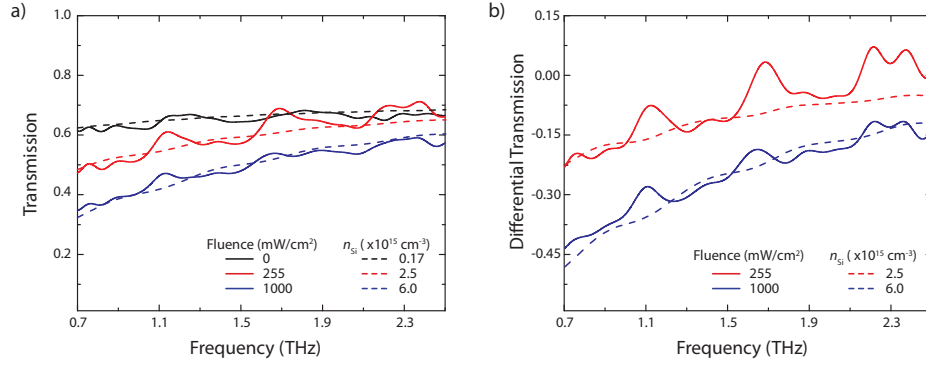


Fig. 2. (a) Solid curves show the transmission of THz radiation through  $\rho$ -Si wafer as a function of frequency for several different optical fluence values. Measurements were done in atmosphere in FTIR system. The dashed curves show the simulated fits for increasing carrier concentration  $n_{Si}$  within the penetration depth (85  $\mu$ m) of  $\rho$ -Si. (b) Dependence of the differential transmission on the optical fluence as defined in the text.

where  $\epsilon_{\infty} = 11.7$  is the frequency independent dielectric permittivity due to the contribution of bound electrons,  $\Gamma = 1/\tau_c$  is the damping rate (with  $\tau_c = 160$  fs the average collision time [28, 31]),  $\omega_p^2$  is the plasma frequency defined as  $\omega_p^2 = n_{Si}e^2/\epsilon_0m^*$  with  $e$  the electron charge,  $\epsilon_0$  the free-space permittivity, and  $m^* = 0.26m_e$  the effective mass [31]. If we neglect the carrier diffusion and consider only free carrier generation and linear recombination in the semiconductor, the carrier density  $n_{Si}$  is proportional to the optical power of the pump beam and is modulated through photodoping [30]

$$n_{Si} = \frac{I_0(1-R)\tau}{2Ad\hbar\omega}, \quad (3)$$

where  $I_0$  is average power,  $R$  is the reflectivity of Si at the pump wavelength,  $\hbar\omega$  is the photon energy,  $\tau = 25$   $\mu$ s is the carrier lifetime [32],  $A$  is the area of the laser excitation, and  $d$  is the penetration depth. At THz frequencies the photodoped charges correspond to a large increase in the absorption coefficient as a function of  $I_0$ , allowing for strong attenuation of incident THz electromagnetic waves.

We measured the THz transmission, shown as the solid curves in Fig. 2, through a 520  $\mu$ m thick  $\rho$ -Si substrate ( $\rho > 10,000$  ohm-cm) for increasing optical power using a 980 nm CW laser diode. We characterize the THz transmission using a Fourier Transform Infrared (FTIR) spectrometer, a mercury (Hg) arc lamp source, multi-layer mylar beamsplitter, and liquid-helium cooled silicon bolometer. The size of the THz and optical beams was 4mm and 9mm, respectively, at the plane where we placed the  $\rho$ -Si substrate. Etalons due to multiple reflections within the  $\rho$ -Si substrate were removed and the modified interferogram was Fourier transformed to obtain the sample spectrum. A similar procedure was performed for a reference with an open channel; division of the sample and reference spectra resulted in the frequency dependent absolute value transmission  $T(\omega)$  and corresponding differential transmission  $[T_p(\omega) - T_{p=0}(\omega)]/T_{p=0}(\omega)$  shown in Figs. 2(a) and 2(b), respectively. We observe broadband attenuation of the THz signal where, at our maximum fluence of  $p = 1$  W/cm<sup>2</sup>, we measure a modulation depth of 43% at 0.7 THz. The undoped ( $T_{p=0}(\omega)$ , black curve) of Fig. 2(a) was performed in vacuum; however, due to technical limitations, transmission measurements for both photodoped cases were performed in air - leading to a reduced signal-to-noise which ac-

counts for the large fluctuations in  $T(\omega)$ .

The dashed curves in Fig. 2 are the results of full wave 3D electromagnetic simulations where we model the resulting change in the transmission as a function of an increase in the  $\rho$ -Si conductivity using the commercial finite difference time domain (FDTD) solver CST Microwave Studio 2012. In simulation we define the  $\rho$ -Si within the penetration depth,  $d = 85 \mu\text{m}$  [28], as a Drude layer, described by Eqs. 2 and 3, with increasing  $n_{Si}$ . Below the penetration depth the  $\rho$ -Si is treated as a dielectric with a constant complex permittivity  $\epsilon_{Si} = 11.7 + 0.01i$ . The photogenerated carrier density approached  $6 \times 10^{15} \text{cm}^{-3}$  for the maximum fluence, in agreement with previous work [28]. The strong frequency dependence of the imaginary component of the dielectric permittivity within the photoexcited region results in high absorption at lower frequencies and minor attenuation above several THz. The qualitative agreement between the model and experimental measurements demonstrate that optically controlled broadband THz modulation is possible. Since the carrier lifetime in  $\rho$ -Si of  $\tau = 25 \mu\text{s}$  is the only fundamental limit to this technique, switching speeds beyond 10 kHz is achievable.

### 3. Experimental setup

A schematic of the THz imaging system is presented in Fig. 3(a) and consists of both an optical beam path (red lines) and a THz beam path (gray lines). As a broadband THz source we utilize a Hg-Arc lamp which emulates a 5500 K blackbody. The source is used in conjunction with a long-pass filter (LPF-065 from Lakeshore) that blocks wavelengths shorter than  $65 \mu\text{m}$  ( $> 4.6 \text{ THz}$ ). The THz imaging optics consist of two 50.8 mm diameter  $90^\circ$  off-axis parabolic mirrors (OAPMs) each with an effective focal length of  $f_L = 190.6 \text{ mm}$ . The first OAPM is  $f_L$  from the source and back-illuminates the object a distance 150 mm away. The second OAPM, a distance 933 mm from the object, focuses the radiation and forms a conjugate image on the SLM 215 mm away. The system has an overall magnification of 0.23, mapping the 43.5 mm diameter object to approximately 10 mm at the SLM. An image was formed by placing a back illuminated patterned metal aperture between the OAPMs so that a THz image (10 mm in diameter) was formed at the SLM plane. The THz image is transmitted through the  $\rho$ -Si and focused using a 50.8 mm diameter TPX lens with  $f = 100 \text{ mm}$  to the detector - a liquid-helium cooled silicon bolometer. The entire apparatus is enclosed and is purged by dry air at room temperature to reduce the THz absorption due to water vapor.

An optical beam is used to spatially modulate the THz image and consists of a 2 W multimode laser diode at a wavelength of 980 nm. An aspheric lens collimates the laser and a Galilean beam expander is used to produce a beam which slightly overfills the DMD. Light is reflected from the DMD in the blaze configuration (described below) and the spatially patterned optical beam is aligned to overlap with the THz image at the front surface of the  $\rho$ -Si wafer achieving a maximum optical fluence of  $250 \text{ mW/cm}^2$ . The DMD shown in Fig. 3(b) is utilized to spatially modulate the optical beam by configuring it as a blazed diffraction grating. Our DMD (DLP D4100-2XLVDS) has a window optimized for the transmission of NIR and  $1024 \times 768$  micro-mirrors (total area  $14.0 \text{ mm} \times 10.5 \text{ mm}$ ), where each mirror has a pitch  $d_{DMD} = 13.68 \mu\text{m}$  and behaves as a binary reflector. By aligning the angle of incidence correctly, the majority of the energy can be directed into the "blazed" order [33]. The blazed condition for wavelength  $\lambda_B$  is related to the grating pitch  $d = d_{DMD}/\sqrt{2}$ , the diffraction order  $m$ , and the facet angle  $\phi = 12^\circ$  as shown in Eq. (4). The fourth blazed angle is centered at  $\lambda = 984 \text{ nm}$  with an efficiency of 47% [34].

$$\lambda_B = \frac{d}{m} \sin 2\phi, \quad (4)$$

The DMD is computer controlled and able to change between frames up to a (software limited) time of 32 ms. Binary bitmap files are loaded into the software to be displayed on the

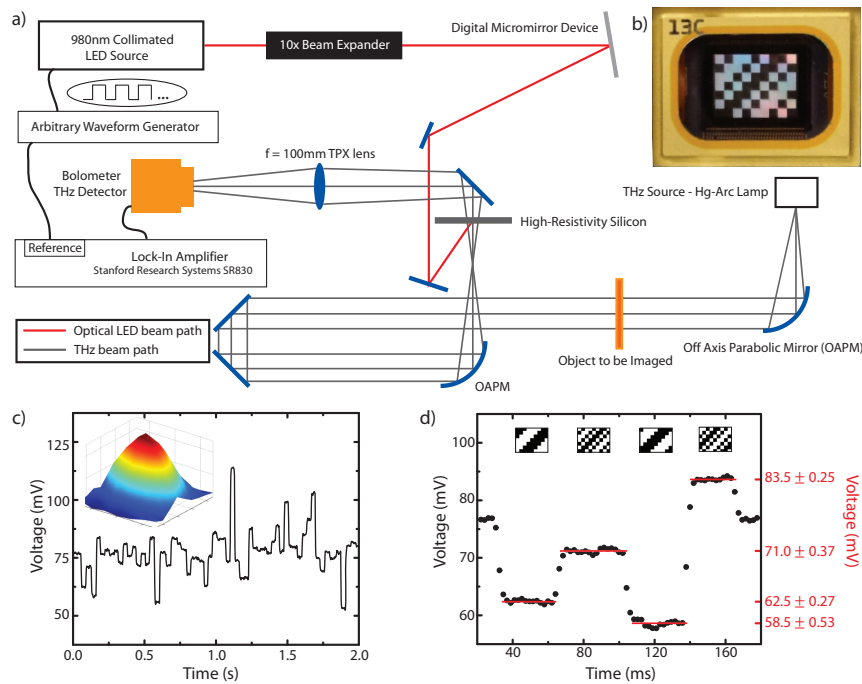


Fig. 3. (a) Schematic of LED and THz optical layouts. The THz beam (shown in gray) passes through the object and is imaged with the OAPMs onto a  $\rho$ -Si wafer. The collimated 980 nm wavelength optical beam (shown in red) reflects off the DMD surface and creates a spatial light pattern at the THz image plane. (b) Photograph of a  $7 \times 9$   $S$ -matrix mask pattern displayed on DMD; each mask pixel is 1.5 mm being constructed from tiling  $109 \times 109$  DMD pixels. (c) Lock-in amplifier voltage output is displayed as a function of time in seconds for the 63 sequential  $S$ -matrix masks; the entire measurement takes approximately 2 s. Inset: reconstructed THz beam profile at image plane. (d) Zoom-in of time data shown in (c). Raw data from four consecutive  $S$ -matrix mask measurements are shown with the corresponding binary mask shown above; the averaged values used for reconstruction along with the standard deviation are shown on the right.

DMD. The white portions represent light that was directed toward the  $\rho$ -Si whereas black represents light that was directed away. This corresponds to white mask regions photodoping the  $\rho$ -Si, i.e. modulating the THz transmission where black represents unmodulated regions. Since the DMD is designed for much shorter optical wavelengths, we may utilize several mirror pixels to function as a single THz-sized pixel for the  $S$ -matrix mask, thus permitting flexibility for both pixel count and pitch. We use  $S$ -matrix masks of varying complexity and change the pixel size accordingly to keep the overall mask area approximately equal. The THz image resolutions we investigated are summarized in Table 1 and the relation between physical size and DMD pixels is detailed.

Table 1. Relationship between THz imaging resolution and DMD pixel sizes

Order ( $N$ )	Resolution	THz Pixel Size	DMD Pixels / THz Pixel
63	$7 \times 9$	$1.5 \text{ mm} \times 1.5 \text{ mm}$	$109 \times 109$
255	$15 \times 17$	$698 \mu\text{m} \times 698 \mu\text{m}$	$51 \times 51$
1023	$31 \times 33$	$328 \mu\text{m} \times 328 \mu\text{m}$	$24 \times 24$

Detection of the THz signal is performed with a lock-in detection technique. The laser diode power is modulated with a square wave at a frequency of 300 Hz, which in turn modulates the THz power detected. Output voltage from the Si-bolometer is input into a lock-in amplifier which provides the measured THz signal in Volts. Figures 3(c), 3(d) show the measured lock-in voltage as a function of time for several successive masks; the corresponding binary bitmap displayed on the DMD are shown above the raw data in Fig. 3(d). The stabilization of the lock-in signal after switching between masks is close to 5 ms, with a SNR recorded for each measurement greater than 100; this is sufficient to allow us to acquire a THz measurement at the limits of the switching time of the DMD. We may estimate the total power of THz radiation used in our imaging apparatus since our bolometer has a calibrated responsivity of  $2.64 \times 10^5$  V/W at 300 Hz. Our DMD may be configured to modulate all pixels on and off, from which we measure a lock-in signal of 130 mV. Thus our THz image consists of a maximum modulated THz power of 96 nW over an integrated bandwidth from 0.2 - 4.6 THz.

#### 4. Experimental results and discussion

Using the experimental apparatus shown in Fig. 3 we performed single pixel THz imaging of various scenes. All THz images are normalized by referencing to the beam profile with no object present. The flexibility afforded by our setup enabled us to image at many different mask resolutions and sizes without physically changing the system. Figure 3(c) shows the THz signal for 63 different  $S$ -matrix masks displayed over a period of 2 s (each mask is displayed for approximately 32 ms). Figure 3(d) shows zoomed-in raw data for consecutive  $S$ -matrix masks, with the corresponding binary mask shown above and the average value used for reconstruction shown in red on the right axis. The inset to Fig. 3(c) shows a false color image of the THz beam profile at the image plane. The reconstruction was done using 63 measurements from the  $7 \times 9$   $S$ -matrix masks (pixel size 1.5 mm) with the total measurement time of approximately 2 s. It is clear from the data shown that quality THz images can be acquired in relatively short times. As stated, the current limitation on speed is software related resulting in mask modulation speed of approximately 31 Hz. However, the response time of the system to a change in mask is approximately 5 ms, resulting in a potential frame rate of 3 fps.

In order to compare our imaging system to more conventional schemes, we perform both raster scan and Hadamard imaging and highlight differences between the two methods - see

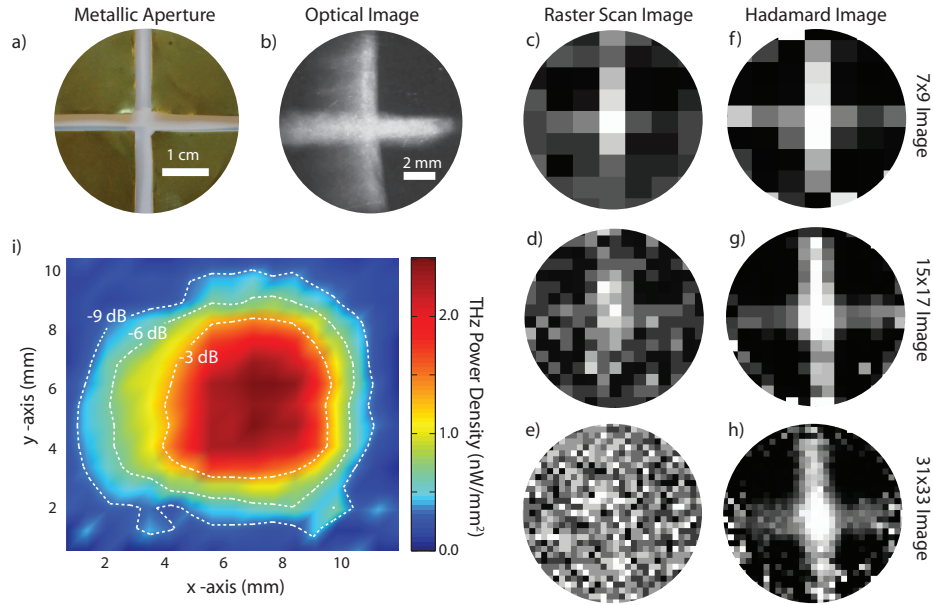


Fig. 4. Comparison of THz imaging with raster scan masks and  $S$ -matrix masks. (a,b) Show the metallic aperture used as the object and the conjugate optical image on the  $\rho$ -Si wafer. (c) Spatial map of the THz power density shown for the reference beam profile with contour plots showing the intensity drop in dB. (d) - (f) Shows raster-scan images for increasing mask complexity. (g) - (i) Shows Hadamard reconstructed images of the same size and complexity as the raster scan measurements to the immediate left. Each mask was displayed for 500 ms for all above measurements.

Fig. 4.  $S$ -matrix masks consist of roughly 50% light throughput and it has been demonstrated that using masks created from an  $N \times N$   $S$ -matrix can increase SNR by a factor of  $\frac{(N+1)}{2\sqrt{N}} \cong \frac{\sqrt{N}}{2}$  over raster scan imaging with the same resolution and pixel size [25]. Figures 4(a), 4(b) show both the metallic aperture used as an object and an optical photograph of the conjugate image at the front surface of the  $\rho$ -Si wafer. It is well known that aspheric optics, such as OAPMs, produce aberrations that can distort the image plane in the form of astigmatism and coma, as seen by the image distortion in Fig. 4(b) [36].

Figures 4(c) – 4(e) show raster-scan images acquired with increasing resolution and constructed from 63, 255, and 1023 measurements respectively. The last column in Fig. 4(f) – 4(h) shows Hadamard reconstructions with the same number of measurements and resolution as the raster scan images. In order to compare different imaging techniques and resolutions, an identical time of 500 ms per mask was used, giving total acquisition times of 31.5 s for the  $7 \times 9$  images, 127.5 s for the  $15 \times 17$  images, and 511.5 s for the  $31 \times 33$  images. While the image quality in the case of  $7 \times 9$  pixel resolution is comparable between the two techniques, the rapid decrease in image quality for the raster scan images at higher resolutions is apparent - see Fig. 4(e). In contrast, the image quality is retained for increasing pixel count in the multiplexing case.

To better understand why the signal depreciated significantly for increasing pixel complexity in the case of the raster scan we investigated the measured power for each respective mask type. We calculate the spatial dependence of the power density ( $\text{nW}/\text{mm}^2$ ) by taking the total measured THz power (96 nW) and extracting the THz power density per pixel  $p_i$  from the

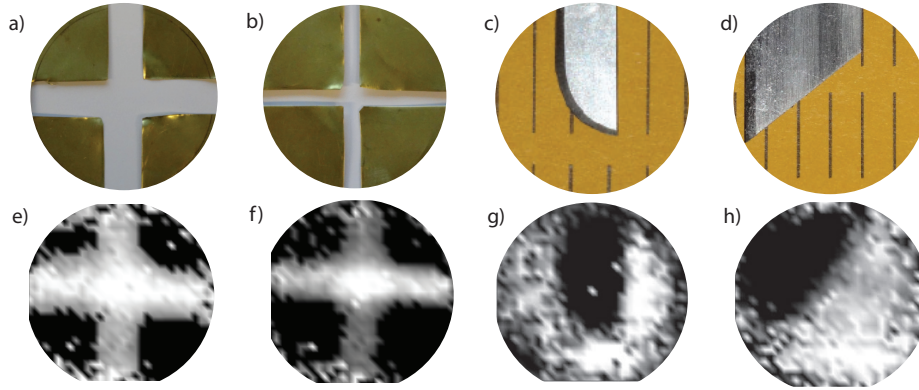


Fig. 5. THz imaging with high-resolution  $S$ -matrix masks ( $31 \times 33$  pixels with each pixel measuring  $328 \mu\text{m}$  on a side). (a,b) Show metallic apertures used as the object of two differently sized crosses, with arm widths of approximately 8 mm and 4.5 mm in the object plane mapping to 2.5 mm and 1.5 mm on the image plane. (c,d) Two different types of metal razor blades that were placed in manila envelopes for imaging. (e) - (h) Shows the THz images of the corresponding objects shown immediately above. Each mask was displayed for 500 ms for all measurements above, giving a total acquisition time of 511.5 s for each image.

measured  $15 \times 17$  beam profile intensity as defined by

$$p_i = \frac{96\text{nW}}{(698\mu\text{m})^2} \times \frac{x_i}{\sum_{i=1}^{255} x_i}, \quad (5)$$

where  $x_i$  is the reconstructed signal from pixel  $i$ . In Fig. 4(i) we show a high quality image of the power density - sufficient to observe optical aberrations resulting from the use of OAPMs which result in an asymmetric distribution of THz power about the horizontal axis, as mentioned above. The power/pixel decreases for increasing resolution since the pixel size is reduced - in our case from 1.5 mm to  $698 \mu\text{m}$  to  $328 \mu\text{m}$ . The peak power density calculated in Eq. (5) is  $2.5 \text{ nW/mm}^2$  near the center of the beam. This corresponds to a total of 5.6 nW of measured power for the 1.5 mm size pixel and 0.27 nW for the  $328 \mu\text{m}$  pixel, a 95% reduction of measured power proportional to the decrease in pixel area. As shown in Fig. 4(i), the power density is -9 dB lower towards the outer diameter of the images and approaches values as low as 50 pW of THz power for  $328 \mu\text{m}$  sized pixels - still well above the bolometer's specified noise-equivalent-power (NEP) of  $1.57 \times 10^{-13} \text{ W}/\sqrt{\text{Hz}}$ . The raster scan is unable to compensate for the loss in measured signal for each pixel due to decreasing pixel dimension. In the Hadamard case, although the signal per pixel also drops with decreasing pixel size, the increase in sampled pixels for each data acquisition offsets the reduction in signal. Consequently, the higher resolution image offers more information without sacrificing SNR. The improvement in the image quality for increasing pixel complexity is evident and allows for the aberrations of the THz image resulting from the OAPMs to be rendered.

In order to explore our imaging technique for possible use in screening applications, in Fig. 5 we show various examples of high-fidelity THz images. The top row displays photographs of all the objects imaged: crosses with 8 mm and 4.5 mm wide arms at the object plane (Fig. 5(a), 5(b)) and two razor blades imaged in manila envelopes (Fig. 5(c), 5(d)). As stated above, we can program the  $S$ -matrix masks to allow for several different functions and mask complexities.

We achieved high resolution images containing  $31 \times 33$  pixels with each mask pixel measuring  $328 \mu\text{m}$  across; this was acquired with 1023 sequential measurements. Like the images shown in Fig. 4, the masks were displayed for 500 ms each, giving a total image acquisition time of 511.5 s. The reconstructed THz images are shown in Fig. 5(e) – 5(h). Due to the magnification of the system, the crosses are imaged down to have 2.5 mm and 1.5 mm wide arms, respectively. The minimum feature size of the images that we can resolve for these crosses is limited by diffraction. The Rayleigh criterion suggests we achieve a diffraction limited spot size of approximately 1.4 mm at 1 THz, although the inherently broadband nature of detected radiation presented here generates a more complex diffraction pattern than that for use of a monochromatic source [35]. The razor blades are placed within manila envelopes and are, obviously, not visible in the optical, however are clearly identified in the THz images, demonstrating the potential for THz imaging to be used in security applications.

## 5. Metamaterial SLMs

Results presented in Figs. 4, 5 demonstrate the ability to perform THz imaging using a single pixel detector. For many potential applications it would be desirable to obtain spectral information, rather than integrating across a portion of the THz range. As discussed in the introduction, metamaterials have shown an ability to modulate THz electromagnetic radiation with demonstrated advantages over conventional materials, including spectral selectivity, amplitude modulation [37], and phase modulation [38]. We computationally explore a metamaterial based SLM which is optically controlled - schematically shown Fig. 6(a). Our metamaterial SLM is modeled similar to that for the  $p$ -Si and we add a complimentary electric split ring resonator [39] to the top of the substrate. The optically excited charge carriers shunt the resonant response of the metamaterial, effectively modulating the transmission at the operational frequency as shown in Figs. 6(b) and 6(c). The metamaterial has been designed to yield a band-pass response centered at 1 THz and achieves a simulated modulation depth of 67% for a maximum fluence of  $1 \text{ W/cm}^2$  - see Fig. 6(b).

The advantage in THz imaging provided by adding resonant metamaterials, as demonstrated in Fig. 6, is an increase in modulation depth at selected frequencies over bare silicon (67% as compared to 37% at 1 THz). The modulation depth could be further improved by optimizing the geometry of  $p$ -Si within the metamaterial unit cell, as well as the photodoping wavelength - both of which could potentially maximize the carrier density closer to the surface. Obtaining spectral information with conventional instruments can be challenging, requiring complex high cost equipment and instrumentation with significantly limited acquisition speeds [40]. By arranging the pixels of metamaterial arrays to have uniquely designed operating frequencies we can create multi-color SLMs that could be used to perform high speed THz spectral imaging offering significant improvement over current systems.

## 6. Conclusion

We have performed high fidelity THz single pixel imaging and various scenes have been rendered. An optically controlled spatial light modulator was implemented through photodoping in high resistivity silicon and controlled by a DMD. We use  $S$ -matrix masks of varying resolution ranging from 63 to 1023 pixels and were able to obtain THz images as fast as one per two seconds. We directly compared Hadamard imaging to the raster-scan technique and highlighted the advantages of the multiplexing method. At THz frequencies dynamically reconfigurable semiconducting device technology provides significant advantages over traditional masks due to the benefit of adaptability and real-time control. This work demonstrates a new path for construction of THz imaging systems. Future work will realize real time imaging of more complex scenes as well as incorporating metamaterials to add additional functionalities applicable to

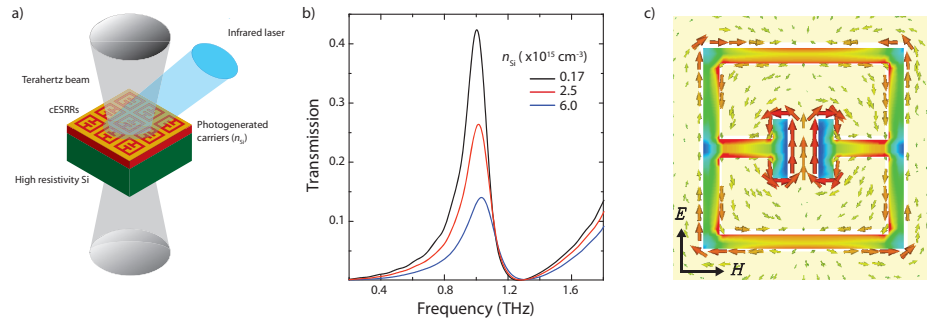


Fig. 6. Optically reconfigurable THz masks with metamaterials. (a) Schematic showing optical pump beam overlapped with THz incident onto complimentary electric split ring resonators (cESRRs) where the photoexcited carriers in Si underneath metamaterial dynamically tune the EM response of the MM. (b) Simulation showing the modulation in THz transmission as a function of carrier excitation. (c) Simulated current density in the cESRR and the electric field magnitude plotted in plane for the case of maximum transmission at 1 THz.

sensing, imaging, and dynamic scene projectors.

### Acknowledgment

The research presented in this work was supported through funding from the Office of Naval Research under US Navy contracts N00014-07-1-0819 (semiconductor modeling) and N00014-11-1-0583 (Hadamard imaging study) and the National Science Foundation under grant ECCS-1002340 (imaging system using digital mirror device).